Intermetallics 144 (2022) 107529

Contents lists available at ScienceDirect

Intermetallics

journal homepage: www.elsevier.com/locate/intermet

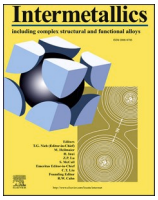

Mechanical behavior of thin CoCrFeNi high-entropy alloy sheet under laser shock peening

J.L. Dong [a], X.Q. Wu [a,*], C.G. Huang [b]

[a] Key Laboratory of Mechanics in Fluid Solid Coupling Systems, Institute of Mechanics, Chinese Academy of Sciences, 100190, Beijing, China
[b] Hefei Institutes of Physical Science, Chinese Academy of Sciences, Hefei, 230031, China

ARTICLE INFO

Keywords:
High-entropy alloy
Mechanical properties
Laser shock peening
Grain refinement
Microstructure evolution

ABSTRACT

It is a challenge to optimize the mechanical performance of high entropy alloys (HEAs). Here, we obtain yield strength enhancement along with considerable tensile ductility of CoCrFeNi HEA by laser shock peening (LSP). The surface hardness of the material is also increased significantly by 40% after LSP. Based on microstructure analysis, it is observed that the grain refinement and the mixed deformation mode of dislocation slip and deformation twin are the main strengthening mechanisms after being treated by LSP. This study demonstrates an effective method for tailoring the mechanical properties of HEAs.

1. Introduction

High-performance metals and alloys with high strength, large plasticity, and strong work-hardening capacity are persistently demanded in a wide range of engineering applications. However, due to the inherent strength-ductility trade-off dilemma of metals, increasing strength usually results in a dramatic loss of ductility. High-entropy alloys (HEAs), a new class of advanced alloys, have attracted great attention in recent years [1,2]. The novel design strategy of multiple principal elements and high-entropy configuration of HEAs provides excellent mechanical properties such as high strength, superior plasticity, exceptional fatigue resistance, and remarkable corrosion resistance [3–5].

Tremendous efforts have been dedicated to tailoring the mechanical performance of HEAs through internal microstructure design, such as the introduction of metastable phase-transformation [6,7], second phase [8,9], gradient hierarchical structures [10,11], and grain refinement [12,13]. In addition, surface treatment techniques play an important role in tailoring the mechanical properties of HEAs. For instance, the aerosol deposition process has been applied successfully to $Fe_{40}(CoCrFeNi)_{60}$ HEA to improve its hardness [14]. Plasma nitriding is also used to improve the mechanical behavior of CoCrFeMnNi HEA [15]. Both the surface Vickers micro-hardness and corrosion resistance improved significantly after the plasma nitriding process.

Laser shock peening (LSP), a powerful surface treatment technique, has been widely employed in aerospace and automobile industries to improve the mechanical behavior of some key components [16,17]. During LSP, a high power density laser transmits through a transparent constraint layer without appreciably energy loss and irradiates a metal thin film on a target. The metal thin film melts, vaporizes, and ionizes under the irradiation of the laser, leading to the formation of plasma. Under the confinement of the confined layer and the target, the pressure of the plasma increases quickly, generating a shock wave with a magnitude of several GPa and a duration of hundreds of nanoseconds in the target [18,19]. If the amplitude of the shock wave exceeds the Hugoniot elastic limit (HEL) of the target, the shocked region of the target deforms severely under ultrahigh strain rates (10^6–$10^7 s^{-1}$), leading to high residual compressive stress and significant improvement of surface mechanical behavior [20]. Lu et al. [21–23] observed the grain refinement induced by surface hardening of the LY2 aluminum alloy, the ANSI 304 stainless steel, and the commercially pure titanium utilizing multiple LSP impacts. Fu et al. [24,25] demonstrated that the LSP impacts facilitated the formation of multiple shear bands and improved the plasticity of Zr-based metallic glasses. Although the mechanical properties of various metals have been improved by LSP [21–34], it is still unknown whether the mechanical behavior of HEAs can be improved by LSP.

In this paper, we performed the LSP treatment on the CoCrFeNi HEAs under different shock conditions. The HEAs exhibit yield strength enhancement and considerable tensile plasticity. In addition, the surface hardness of the material is increased significantly after LSP. The microstructure evolutions are also characterized to reveal the underlying mechanism of the HEAs after LSP.

* Corresponding author.
E-mail address: wuxianqian@imech.ac.cn (X.Q. Wu).

https://doi.org/10.1016/j.intermet.2022.107529
Received 25 November 2021; Received in revised form 17 February 2022; Accepted 1 March 2022
Available online 5 March 2022

2. Materials and methods

The equiatomic CoCrFeNi ingot was synthesized via arc-melting under a Ti-getter argon atmosphere with high purity constituent elements (purity >99.9 wt %). To ensure the chemical homogeneity, the ingot was re-melted at least four times before being drop-casted into a cooper mold with a dimension of 85 × 10 × 2 mm to obtain the HEA bulk sample. The sample thickness was reduced to 0.5 mm by cold-rolling and the plates were then annealed at 1200 K for 2 h to ensure full recrystallization, followed by water-quenching. An electrical discharge machine was used to section the rectangular dog-bone specimens from the recrystallized sheets, with the tensile axis oriented along the rolling direction. The gage dimensions of tensile specimens were 10 × 3.5 × 0.5 mm.

The bulk samples and the dog-bone specimens were mechanically polished to reduce the influence of surface roughness using SiC papers (from #400 to #2000). The tensile tests were carried out at room temperature with an Instron 5969 testing machine at the strain rate of 5×10^{-3} s^{-1}. Micro-hardness testing was performed with an HXD 1000TMSC/LCD Vickers indenter. During the micro-hardness test, the load is 0.98 N, the duration is 10 s, and the indentation size is 3 × 3 μm right square pyramid. Three bulk samples are treated for each LSP condition, and the micro-hardness of each sample is measured, yielding the average micro-hardness value. X-ray diffraction (XRD) measurements (Ultima IV) were conducted on the untreated and the LSP-treated tensile specimens (laser power density: 2.83 GW/cm^2) to identify the phase structures. The microstructural characteristics and texture information were examined using a scanning electron microscope (SEM) equipped with electron backscatter diffraction (EBSD) on a JEOL JSM-7100F field emission gun-SEM. The specimen surfaces for EBSD were mechanically polished first, and then polished with a 0.05 μm SiO_2 aqueous suspension, followed by electro-polished at 37 V in a solution of 5% $HClO_4$ and 95% alcohol. The refined microstructures were analyzed by a JEM-2100 transmission electron microscopy (TEM) to uncover the underlying deformation mechanisms. Thin disks were mechanically polished to about 30 μm before being ion milled to perforation at room temperature for TEM observations.

The developed LSP platform is illustrated in Fig. 1(a). The shocking surface of the target is firstly cemented with a 40-μm-thick aluminum (Al) film as an absorbing layer to protect the target surface from thermal ablation. Since the deionized water possesses high light transmittance, it is used as a confining layer to constrain the plasma generated by laser irradiation. A single laser pulse with an FWHM of 10 ns and 1064 nm wavelength excited by a Q-switched Nd:YAG laser is focused into a 3-mm-diameter spot size on the Al film. The energy of the pulsed laser is adjusted to about 0.5, 1, 1.5, and 2 J to investigate the influence of the laser energy, and the corresponding laser power densities irradiated at the target surface are estimated to be 0.71, 1.41, 2.12, and 2.83 GW/cm^2, respectively. The peak pressure induced by a laser pulse is estimated by Fabbro's model [28],

$$p_m(GPa) = 0.01\sqrt{\alpha/(2\alpha+3)}\sqrt{Z(g\ cm^{-2}s^{-1})}\sqrt{I_0(GW\ cm^{-2})}, \quad (1)$$

where α is the fraction of absorbed energy contributed by the thermal energy ($\alpha = 0.25$), I_0 is the laser power density. Z is the reduced shock impedance between the constraint layer (purified water, shock impedance: 1.418×10^6 g·cm^{-2}s^{-1}) and the absorption layer (Al film, shock impedance: 1.47×10^6 g·cm^{-2}s^{-1}). The peak pressures generated by laser-induced shock are calculated in a range of 2.7–5.39 GPa for laser power densities from 0.71 to 2.83 GW/cm^2, respectively. The laser energy, spot size, power density, and peak pressure are listed in Table 1.

Fig. 1(b) depicts the laser impact trajectory of the specimen. Generally, multiple LSP impacts can lead to a relatively uniform distribution of the residual stresses. However, the overlap ratio of laser shots has a crucial influence on the strengthening effect. As the overlap ratio increases, the stress amplitude in the impact area will initially increase and then decrease. A larger compressive stress amplitude can be obtained when the overlap ratio of laser shots is about 50% [35]. Thus, a 50% overlap ratio of laser shots is employed and realized by a high-precision X–Y stage in the present study. The EBSD and TEM specimens were collected from the second shock region, as depicted in Fig. 1(b).

3. Results and discussion

We first perform the LSP on the bulk sample with a thickness of 2 mm to determine the plastically affected depth. Fig. 2(a) shows the distribution of the micro-hardness on the cross-section of the LSP-treated bulk sample versus depth. Obviously, the hardness of the specimen increases with the increase of laser power density. At 2.83 GW/cm^2, the surface hardness of the specimen increases significantly by 40% when compared to that of the untreated specimen. At a depth of about 650 μm, the measured hardness decreases to the hardness value of the untreated specimen, indicating that the plastically affected depth is about 650 μm. The significant increase of hardness should be mainly attributed to the high dislocation density near the shocked surface resulting from the

Table 1
Laser energy, power density, and peak pressure of the LSP for treating HEAs.

Laser energy (J)	Laser spot diameter (mm)	Power density (GW/cm^2)	Peak pressure (GPa)
0.5	3	0.71	2.7
1	3	1.41	3.8
1.5	3	2.12	4.66
2	3	2.83	5.39

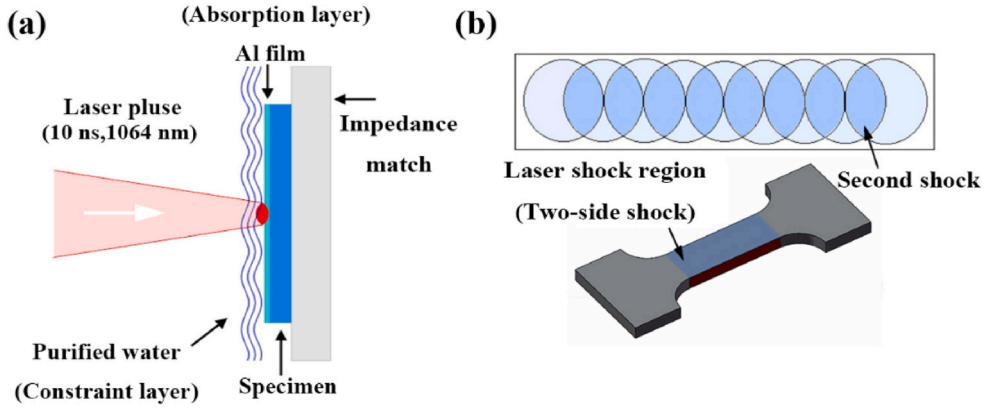

Fig. 1. (a) Schematic diagram of the LSP impacts platform. (b) Laser impact trajectory and laser spot overlap of the tensile specimen.

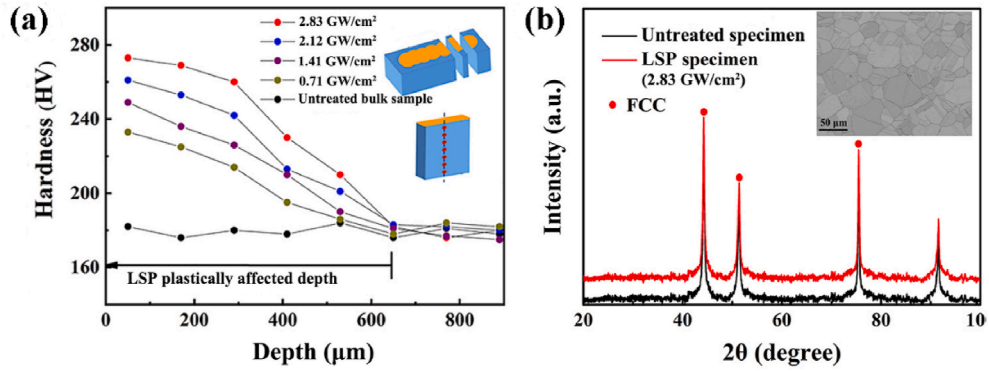

Fig. 2. (a) Vickers hardness-dependent depth on the cross-section of LSP-treated specimen, the inset is the scanning schematic for the Vickers hardness measurement. (b) XRD profiles of the untreated and LSP-treated specimen, the inset is the microstructures of the untreated specimen.

severe plastic deformation during LSP. Fig. 2(b) shows the XRD profiles of untreated and LSP-treated (power density 2.83 GW/cm^2) HEAs, indicating a single face-centered cubic (FCC) solid-solution phase structure without any phase transition after LSP impacts. The inset in Fig. 2(b) displays the annealed specimen (untreated) with a fully recrystallized microstructure and several annealing twins.

Fig. 3(a) shows the tensile stress-strain curves of the untreated and LSP-treated specimens at the strain rate of 5×10^{-3} s^{-1}. It can be seen that the untreated specimens show a yield strength of 220 MPa and uniform tensile elongation of ~70%. The LSP-treated specimens have a significant increase in both yield strength and ultimate tensile strength when compared to that of the untreated specimen. Furthermore, the large elongation property almost remains after LSP. At 2.83 GW/cm^2, the LSP-treated specimen exhibits excellent mechanical behavior with the yield strength of 440 MPa, the ultimate tensile strength of 650 MPa, and the plastic strain of 50%. Fig. 3(b) summarizes the yield strength, ultimate tensile strength, and fracture tensile elongation with respect to the laser power density. The yield strength and ultimate tensile strength increase almost linearly as the laser power density increase, while the fracture tensile elongation decreases slightly. At 2.83 GW/cm^2, the yield strength of the LSP-treated specimens increases by 100%, and the fracture tensile elongation decreases by 28% when compared to that of the untreated specimens. The experimental results indicate that LSP is capable of optimizing the mechanical properties of HEAs. According to the previous studies [21–24,29,32–34], the excellent mechanical behavior of the CoCrFeNi HEAs should be mainly ascribed to the evolution of microstructure induced by LSP.

Fig. 4 shows the EBSD results of the untreated and LSP-treated specimens (laser power density: 2.83 GW/cm^2). As shown in Fig. 4(a), the inverse pole figure (IPF) of the untreated specimen indicates a fully recrystallized microstructure with randomly oriented and equiaxed grains and a few microscale annealing twins. The EBSD IPF map of the LSP-treated specimen is presented in Fig. 4(b). Obviously, the grains are refined and show the preferred orientation along <111> (blue) and <101> (green), which is different from the randomly orientated grains of the untreated specimen. The texture towards <111> is the typical texture owing to the grain rotation after severe plastic deformation in FCC metals and alloys like twin induced plasticity (TWIP) steels [36]. The fraction of the recrystallized region is measured to 9.7% in the LSP-treated specimen (see supplementary materials, Fig. S1). Fig. 4(c and d) are the grain boundary maps. The untreated specimen contains a few low-angle grain boundaries (LAGBs, with misorientation <10°) (Fig. 4(c)). Fig. 4(d) shows that a large number of LAGBs are formed in the LSP-treated specimen, implying that the multiplication, interaction, and trapping of dislocations are extensively activated inside the LSP-induced refined grain. Fig. 4(e and f) exhibit the grain size distributions of the untreated and LSP-treated specimens in terms of the area fraction. High-angle grain boundaries (HAGBs, with misorientation >10°) and twin boundaries are counted when calculating the grain size due to the similar inhibition effect for dislocation movement. The average grain sizes of the untreated and the LSP-treated specimen are 30 ± 5 μm and 20 ± 3 μm, respectively, showing an obvious grain refinement after LSP. According to the Hall-Petch relationship, grain refinement is an effective method to improve the strength of materials. The grain boundary is the obstacle to dislocation movement. Thus, higher stress is required for dislocation slip in fine-grain metals and therefore the material is strengthened. We also conducted the EBSD in the cross-section of the LSP-treated specimen, as shown in Fig. 4(g). The result exhibits a relatively homogeneous microstructure in the LSP-treated specimen.

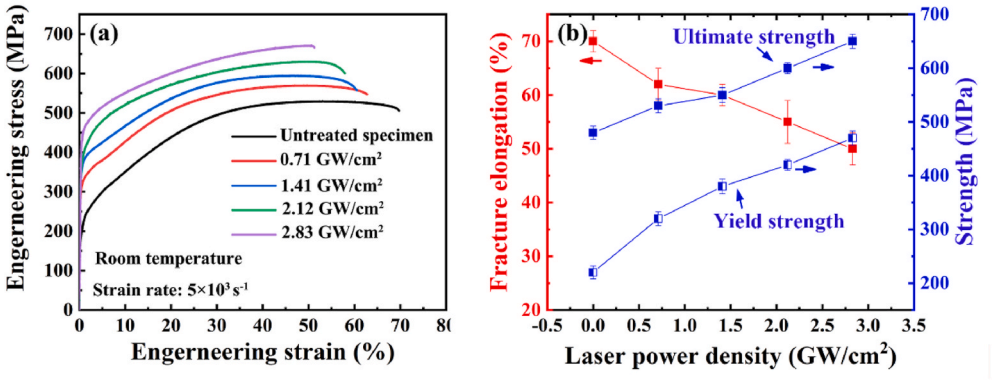

Fig. 3. (a) Engineering stress-strain curves of the untreated and the LSP-treated specimens under quasi-static tension. (b) Fracture elongation, yield strength, and ultimate strength of the untreated and the LSP-treated specimen under quasi-static tension.

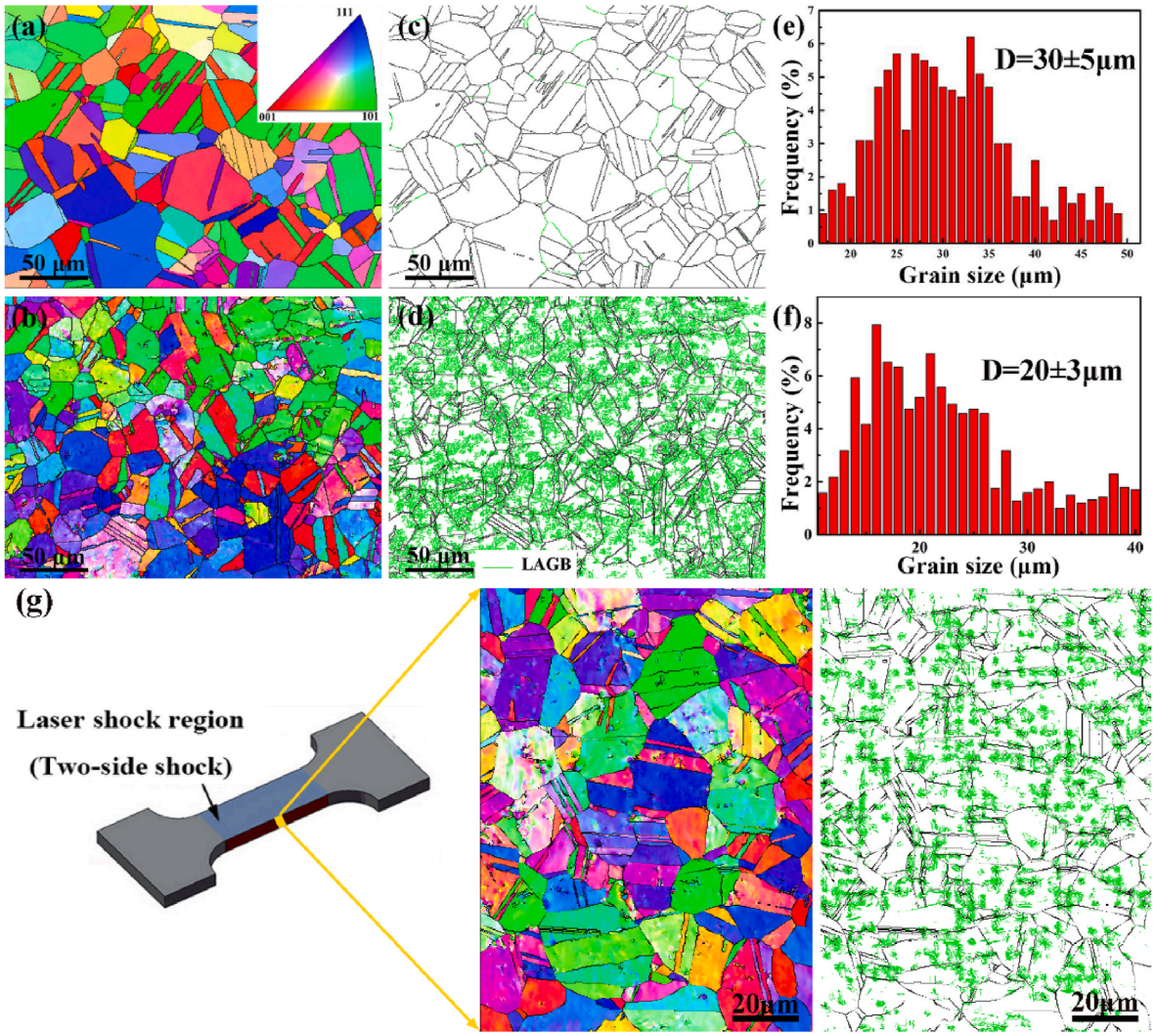

Fig. 4. EBSD results for untreated and LSP-treated specimens (laser power density: 2.83 GW/cm^2). (a–b) EBSD IPF maps. (c–d) Grain boundary maps showing the LAGBs. (e–f) Grain size distribution plotted in terms of the area fraction. (g) EBSD IPF maps and grain boundary maps of LSP-treated tensile specimens along the thickness direction.

Similar grain refinement has been observed in ANSI 304 stainless steel (from 7-10 μm to 1–2 μm) [23], LY2 Al alloy (from 10 μm to 3–5 μm) [21], commercially pure titanium [22], and HEA (from 98 μm to 56 μm) [32–34] after multiple LSP impacts, where severe plastic deformation under ultrahigh strain rates plays a crucial role. Based on the study by Lu et al. [21–23], the grain refinement process during LSP can be described as follows: (i) formation and development of dislocation lines in original grains; (ii) dislocation tangles; (iii) transformation of dislocation tangles into subgrain boundaries; (iv) evolution of the continuous dynamic recrystallization in subgrain boundaries to refined grain boundaries. The very fine microstructures cannot be characterized due to the resolution limit of the EBSD. Therefore, the TEM with the higher spatial resolution is also performed to explore the microstructure evolution of the LSP-treated specimen.

A series of bright-field TEM images of the LSP-treated specimens under different laser power densities are shown in Fig. 5. Four typical LSP-induced microstructure features, i.e. dislocation tangles, planar slip, stacking faults, and deformation twins are identified. As shown in Fig. 5 (a), the high-dense dislocation tangles can be visibly observed under the laser power density of 0.71 GW/cm^2. With increasing the laser power density to 1.41 GW/cm^2, the typical dislocation slip occurs as shown in Fig. 5(b), indicating that the dislocation tangles associated with planar slip are the main deformation mechanism in the relatively low laser power density. A similar dislocation structure with planar slip was found in $Fe_{40}Mn_{40}Co_{10}Cr_{10}$ and CoCrFeMnNi HEAs upon loadings [37,38]. As the continuous increase of the laser power densities to 2.12 and 2.83 GW/cm^2, high density stacking faults (SFs) and deformation twins (DTs) as evidenced by the corresponding selected area electron diffraction (SEAD) pattern along zone axis Z = [011] in the inset of Fig. 5(d) are exhibited in Fig. 5(c) and (d), respectively, indicating the mixed deformation mode of dislocation slip and DTs in the HEA at high shock pressures. The SFs and DTs induced by the LSP have two-fold effects for the strengthening of the HEA. First, the pre-existing DTs and SFs can introduce a new subgrain boundary and decrease the mean free path of dislocations during tensile tests (dynamic Hall-Petch effect), producing a significant increase in strength [39]. Second, the smaller grain size and the pre-existing DTs avoid the localized plasticity and delay the necking onset during tension tests, providing a good ductility and strong work hardening capacity. The excellent mechanical behavior is achieved by LSP, which can be attributed to the transformation of deformation mechanisms from the dislocation-dominated mode in the untreated specimen to the various deformation mechanisms including dislocations, SFs, and DTs in LSP-treated specimen.

Since the significant increase of the yield strength of the LSP-treated CoCrFeNi HEA is attributed to the pre-existing dislocations and DTs in the fine grain, the increase of yield strength ($\Delta\sigma_Y$) can be considered as

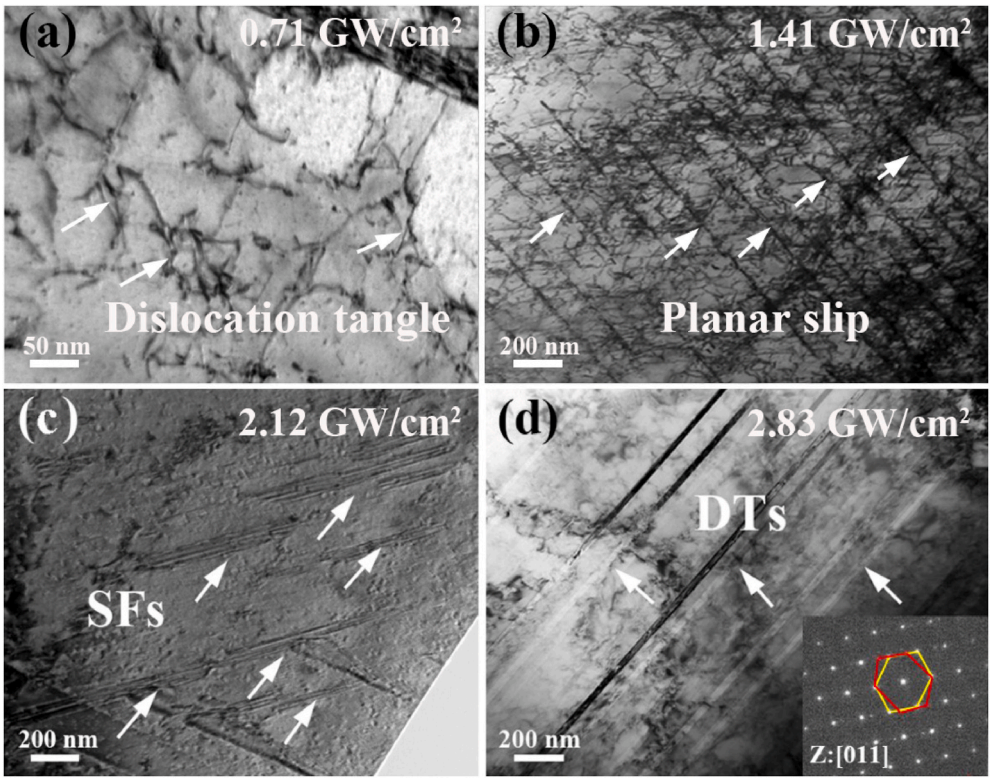

Fig. 5. TEM image showing the different microstructures induced by LSP. (a) plane slip; (b) dislocation tangles; (c) stack faults; (d) deformation twins.

the superposition of the strength contributions from twin boundaries ($\Delta\sigma_T$), dislocations ($\Delta\sigma_D$), and grain refinement ($\Delta\sigma_G$) [40],

$$\Delta\sigma_Y = f_R\Delta\sigma_G + (1-f_R)\Delta\sigma_D + \Delta\sigma_T, \quad (2)$$

where $f_R = 9.7\%$ is the fraction of the recrystallized region. $\Delta\sigma_G$ has the following Hall-Petch relationship [41,42],

$$\Delta\sigma_G = k_g d^{-\frac{1}{2}}, \quad (3)$$

where the strengthening coefficient, k_g, for the present HEA is 494 MPa $\mu m^{\frac{1}{2}}$[42], d is the average grain size of about 20 μm as shown in Fig. 4(f). The strengthening effect of dislocations ($\Delta\sigma_D$) is generally evaluated as [43],

$$\Delta\sigma_D = M\alpha Gb\sqrt{\rho}, \quad (4)$$

where M is the average Taylor factor ($M = 3.06$), α is a constant ($\alpha = 0.2$), G is shear modulus ($G = 81$ GPa), b is Burgers vector ($b = \frac{\sqrt{2}}{2}a = 2.52 \times 10^{-10}$m), and the dislocation density ρ is estimated to be around $2.295 \times 10^{14}/m^2$ (see supplementary material, Fig. S2). The strengthening effect of twins can be evaluated as [44],

$$\Delta\sigma_T = fk_t\lambda^{-\frac{1}{2}}, \quad (5)$$

where $f = 2\%$ is the volume fraction of twin (see supplementary material), $k_t = 195$ MPa $\mu m^{\frac{1}{2}}$ is the strengthening factor by twin boundaries [45], λ is the average distance between twins (λ = 4 μm, Fig. 4(b)).

The strengthening contributions of grain boundary, dislocation, and deformation twins are calculated as 110, 190, and 1.95 MPa, respectively. Therefore, the increase of the yield strengthening is estimated to be 185 MPa based on Eq. (2). The error between the calculated value (185 MPa) and the experiment result (220 MPa) is less than 20%, validating the estimation method of the strengthening effects by LSP.

4. Conclusions

In this paper, the mechanical properties and microstructure evolution of CoCrFeNi HEAs under LSP are investigated. The main conclusions are as follows.

(1) The surface hardness of the HEA is increased by 40% under LSP with laser power density of 2.83 GW/cm^2, and the maximum plastically affected depth is about 650 μm.
(2) LSP is an effective method to improve the mechanical behavior for the HEA. After LSP with laser power density 2.83 GW/cm^2, the yield strength increases by 100%, and the tensile elongation decrease by 28% when compared to that of the untreated HEA.
(3) A large number of LAGBs are obtained, and the grains of the HEA are obviously refined after LSP.
(4) Grain refinement and mixed deformation mode of dislocation slip and deformation twin are the main strengthening mechanisms for the LSP-treated HEAs.

Author statement

J.L. Dong: Conceptualization, Formal analysis, Resources and Writing—original draft.; X.Q. Wu: Conceptualization, Writing—review and editing and Supervision.; C.G. Huang: Supervision.;

Declaration of competing interest

The authors declare that they have no known competing financial interests or personal relationships that could have appeared to influence the work reported in this paper.

Acknowledgment

This work was supported by the National Natural Science Foundation of China (Nos. 11772347), Science Challenge Project (grant no.

TZ2018001), and the Strategic Priority Research Program of the Chinese Academy of Sciences (Nos. XDB22040302 and XDB22040303).

Appendix A. Supplementary data

Supplementary data to this article can be found online at https://doi.org/10.1016/j.intermet.2022.107529.

References

[1] J.W. Yeh, S.K. Chen, S.J. Lin, J.Y. Gan, Nanostructured high-entropy alloys with multiple principal elements: novel alloy design concepts and outcomes, Adv. Eng. Mater. 6 (5) (2004) 299–303.

[2] B. Cantor, I. Chang, P. Knight, A. Vincent, Microstructural development in equiatomic multicomponent alloys, Mater. Sci. Eng. A 375 (2004) 213–218.

[3] Z. Yong, T.T. Zuo, T. Zhi, M.C. Gao, K.A. Dahmen, P.K. Liaw, P.L. Zhao, Microstructures and properties of high-entropy alloys, Prog. Mater. Sci. 61 (2014) 1–93.

[4] T.W. Zhang, S.G. Ma, D. Zhao, Y.C. Wu, Y. Zhang, Z.H. Wang, J.W. Qiao, Simultaneous enhancement of strength and ductility in a NiCoCrFe high-entropy alloy upon dynamic tension: micromechanism and constitutive modeling, Int. J. Plast. 124 (2020) 226–246.

[5] G. Bernd, H. Anton, C. Dhiraj, E.H. Chang, E.P. George, R.O. Ritchie, A fracture-resistant high-entropy alloy for cryogenic applications, Science 345 (6201) (2014) 1153.

[6] Z. Li, K.G. Pradeep, Y. Deng, D. Raabe, C.C. Tasan, Metastable high-entropy dual-phase alloys overcome the strength–ductility trade-off, Nature 534 (2016) 227–230.

[7] H. Huang, Y. Wu, J. He, H. Wang, X. Liu, K. An, W. Wu, Z. Lu, Phase-transformation ductilization of brittle high-entropy alloys via metastability engineering, Adv. Mater. 29 (30) (2017), 1701678.1-1701678.7.

[8] K. Ming, X. Bi, J. Wang, Realizing strength-ductility combination of coarse-grained $Al_{0.2}Co_{1.5}CrFeNi_{1.5}Ti_{0.3}$ alloy via nano-sized, coherent precipitates, Int. J. Plast. 100 (2018) 177–191.

[9] B. Gwalani, V. Soni, M. Lee, S.A. Mantri, Y. Ren, R. Banerjee, Optimizing the coupled effects of Hall-Petch and precipitation strengthening in a $Al_{0.3}$CoCrFeNi high entropy alloy, Mater. Des. 121 (2017) 254–260.

[10] G. Chen, J.W. Qiao, Z.M. Jiao, D. Zhao, T.W. Zhang, S.G. Ma, Z.H. Wang, Strength-ductility synergy of $Al_{0.1}$CoCrFeNi high-entropy alloys with gradient hierarchical structures, Scripta Mater. 167 (2019) 95–100.

[11] M.X. Yang, D.S. Yan, F.P. Yuan, P. Jiang, E. Ma, Dynamically reinforced heterogeneous grain structure prolongs ductility in a medium-entropy alloy with gigapascal yield strength, Proc. Natl. Acad. Sci. Unit. States Am. (2018) 1–6.

[12] B. Schuh, F.M. Martin, B. Volker, E.P. George, Mechanical properties, microstructure and thermal stability of a nanocrystalline CoCrFeMnNi high-entropy alloy after severe plastic deformation, Acta Mater. 96 (2015) 258–268.

[13] J. Yang, J.W. Qiao, S.G. Ma, G.Y. Wu, D. Zhao, Z.H. Wang, Revealing the Hall-Petch relationship of Al0.1CoCrFeNi high-entropy alloy and its deformation mechanisms, J. Alloys Compd. 795 (2019) 269–274.

[14] T.A. Listyawan, A. Kumar, W. Shin, H. Do, K.H. Lee, J. Ryu, N. Park, Surface hardening treatment of $Fe_{40}(CoCrMnNi)_{60}$ medium entropy alloy via aerosol deposition technique: a new approach, Mater. Lett. 269 (15) (2020) 127633.

[15] N. Akio, F. Takahiro, M. Toru, Microstructural, mechanical, and corrosion properties of plasma-nitrided CoCrFeMnNi high-entropy alloys, Surf. Coating. Technol. 376 (25) (2018) 52–58.

[16] P. Peyre, R. Fabbro, Laser shock processing: a review of the physics and applications, Opt. Quant. Electron. 27 (12) (1995) 1213–1229.

[17] P. Peyre, X. Scherpereel, L. Berthe, R. Fabbro, Current trends in laser shock processing, Surf. Eng. 14 (5) (1998) 377–380.

[18] L. Berthe, R. Fabbro, P. Peyre, L. Tollier, E. Bartnicki, Shock waves from a water-confined laser-generated plasma, J. Appl. Phys. 82 (6) (1997) 2826–2832.

[19] R. Fabbro, J. Fournier, P. Ballard, D. Devaux, J. Virmont, Physical study of laser-produced plasma in confined geometry, J. Appl. Phys. 68 (2) (1990) 775–784.

[20] C.S. Montross, T. Wei, L. Ye, G. Clark, Y.W. Mai, Laser shock processing and its effects on microstructure and properties of metal alloys: a review, Int. J. Fatig. 24 (10) (2002) 1021–1036.

[21] J.Z. Lu, K.Y. Luo, Y.K. Zhang, C.Y. Cui, G.F. Sun, J.Z. Zhou, L. Zhang, J. You, K. M. Chen, J.W. Zhong, Grain refinement of LY2 aluminum alloy induced by ultra-high plastic strain during multiple laser shock processing impacts, Acta Mater. 58 (11) (2010) 3984–3994.

[22] J.Z. Lu, L.J. Wu, G.F. Sun, K.Y. Luo, Y.K. Zhang, J. Cai, C.Y. Cui, X.M. Luo, Microstructural response and grain refinement mechanism of commercially pure titanium subjected to multiple laser shock peening impacts, Acta Mater. 127 (2017) 252–266.

[23] J.Z. Lu, K.Y. Luo, Y.K. Zhang, G.F. Sun, Y.Y. Gu, J.Z. Zhou, X.D. Ren, X.C. Zhang, L. F. Zhang, K.M. Chen, C.Y. Cui, Y.F. Jiang, A.X. Feng, L. Zhang, Grain refinement mechanism of multiple laser shock processing impacts on ANSI 304 stainless steel, Acta Mater. 58 (16) (2010) 5354–5362.

[24] J. Fu, Y. Zhu, C. Zheng, R. Liu, Z. Ji, Evaluate the effect of laser shock peening on plasticity of Zr-based bulk metallic glass, Opt Laser. Technol. 73 (2015) 94–100.

[25] J. Fu, Y. Zhu, C. Zheng, R. Liu, Z. Ji, Effect of laser shock peening on mechanical properties of Zr-based bulk metallic glass, Appl. Surf. Sci. 313 (2014) 692–697.

[26] A. Umapathi, S. Swaroop, Deformation of single and multiple laser peened TC6 titanium alloy, Opt Laser. Technol. 100 (2018) 309–316.

[27] M.Z. Ge, J.Y. Xiang, Z. Fan, Y.L. Lu, W.N. Lei, Effect of laser energy on microstructure of Mg-3Al-1Zn alloy treated by LSP, J. Alloys Compd. 734 (2018) 266–274.

[28] X. Wang, W. Xia, X. Wu, Y. Wei, C. Huang, In-situ investigation of dynamic deformation in NiTi shape memory alloys under laser induced shock, Mech. Mater. 114 (2017) 69–75.

[29] M.Z. Ge, J.Y. Xiang, L. Yang, J.T. Wang, Effect of laser shock peening on the stress corrosion cracking of AZ31B magnesium alloy in a simulated body fluid, Surf. Coating. Technol. 310 (2017) 157–165.

[30] P. Peyre, R. Fabbro, P. Merrien, H.P. Lieurade, Laser shock processing of aluminium alloys. Application to high cycle fatigue behaviour, Mater. Sci. Eng. A 210 (1–2) (1996) 102–113.

[31] P. Peyre, L. Berthe, X. Scherpereel, R. Fabbro, E. Bartnicki, Experimental study of laser-driven shock waves in stainless steels, J. Appl. Phys. 84 (11) (1998), 5985-5985.

[32] Z. Tong, X. Pan, W. Zhou, Y. Yang, X. Ren, Achieving excellent wear and corrosion properties in laser additive manufactured CrMnFeCoNi high-entropy alloy by laser shock peening, Surf. Coating. Technol. 422 (80) (2021) 127504.

[33] Z. Tong, H. Liu, J. Jiao, W. Zhou, X. Ren, Improving the strength and ductility of laser directed energy deposited CrMnFeCoNi high-entropy alloy by laser shock peening, Addit. Manuf. 35 (2020) 101417.

[34] Z. Tong, H. Liu, J. Jiao, W. Zhou, X. Ren, Microstructure, microhardness and residual stress of laser additive manufactured CoCrFeMnNi high-entropy alloy subjected to laser shock peening, J. Mater. Process. Technol. 285 (2020) 116806.

[35] X. Wu, Q. Tan, C. Huang, Geometrical scaling law for laser shock processing, J. Appl. Phys. 114 (4) (2013) 1021–1036.

[36] I. Gutierrez Urrutia, D. Raabe, Multistage strain hardening through dislocation substructure and twinning in a high strength and ductile weight-reduced Fe–Mn–Al–C steel, Acta Mater. 60 (16) (2012) 5791–5802.

[37] Y. Deng, C.C. TaSan, K.G. Pradeep, H. Springer, A. Kostka, D. Raabe, Design of a twinning-induced plasticity high entropy alloy, Acta Mater. 94 (2015) 124–133.

[38] G. Laplanche, A. Kostka, O.M. Horst, G. Eggeler, E.P. George, Microstructure evolution and critical stress for twinning in the CrMnFeCoNi high-entropy alloy, Acta Mater. 118 (2016) 152–163.

[39] B.C. De Cooman, Y. Estrin, S.K. Kim, Twinning-induced plasticity (TWIP) steels, Acta Mater. 142 (2018) 283–362.

[40] H.T. Wang, N.R. Tao, K. Lu, Strengthening an austenitic Fe–Mn steel using nanotwinned austenitic grains, Acta Mater. 60 (9) (2012) 4027–4040.

[41] H. Wen, T.D. Topping, D. Isheim, D.N. Seidman, E.J. Lavernia, Strengthening mechanisms in a high-strength bulk nanostructured Cu–Zn–Al alloy processed via cryomilling and spark plasma sintering, Acta Mater. 61 (8) (2013) 2769–2782.

[42] W.H. Liu, Y. Wu, J.Y. He, T.G. Nieh, Z.P. Lu, Grain growth and the Hall–Petch relationship in a high-entropy FeCrNiCoMn alloy, Scripta Mater. 68 (7) (2013) 526–529.

[43] G. Dini, R. Ueji, A. Najafizadeh, S.M. Monir-Vaghefi, Flow stress analysis of TWIP steel via the XRD measurement of dislocation density, Mater. Sci. Eng. A 527 (10–11) (2010) 2759–2763.

[44] I.G. Urrutia, D. Raabe, Dislocation and twin substructure evolution during strain hardening of an Fe–22 wt.% Mn–0.6 wt.% C TWIP steel observed by electron channeling contrast imaging, Acta Mater. 59 (16) (2011) 6449–6462.

[45] J. Su, D. Raabe, Z. Li, Hierarchical microstructure design to tune the mechanical behavior of an interstitial TRIP-TWIP high-entropy alloy, Acta Mater. 163 (1) (2019) 40–54.